2020

Formation of p-n Junctions in Nanoparticle Cerium Oxide Electrolytic Cells Displaying Memristive Switching Behaviour

Rafaela Cristina De Carvalho
Technological University Dublin, rafa_cdc@hotmail.com

Tony Betts
Technological University Dublin, anthony.betts@tudublin.ie

John Cassidy
Technological University Dublin, john.cassidy@tudublin.ie

Recommended Citation

de Carvalho, R.C., Betts, T. & Cassidy, J.F. (2020) Formation of p-n Junctions in Nanoparticle Cerium Oxide Electrolytic Cells Displaying Memristive Switching Behaviour, *Phys. Chem. Chem. Phys.*, 2020,22, 4216-4224 . DOI:10.1039/C9CP06016B

Formation of p-n Junctions in Nanoparticle Cerium Oxide Electrolytic Cells Displaying Memristive Switching Behaviour

Rafaela C. de Carvalho[a,b], Anthony J. Betts[a,c], John F. Cassidy [a, b]

A macro-scale metal-semiconductor-metal device comprising CeO_2 nanoparticles cast from a suspension of cerium dioxide formed by a novel synthetic method was fabricated. Thin CeO_2 films of 40 nm thickness placed between panels of aluminium and/or copper displayed memristive-like resistive switching behaviour upon the application of potential sweeps ranging between -0.6 V and 0.6 V. A mechanism is proposed based on the notion that an electrolytic cell operates under such conditions with the initial formation of p and n-type regions within the central semiconductive thin film. Evidence is presented for the existence of numerous point defects in these nanosized CeO_2 films, which are also likely to play a role in the device's operation acting as internal dopants. Steady currents were observed upon the imposition of constant potentials, most notably at higher potential values (both anodic and cathodic). It is suggested that electrons and holes act as charge carriers in these devices rather than ionic species as proposed in some other mechanisms.

1. Introduction

Resistive Random-Access Memory (RRAM also known as ReRAM) is a resistive switching memory and has been proposed as one of the next generation of non-volatile memory technologies for the computing industry. It is normally constructed from a metal/semiconductor/metal configuration (MSM), often with a transition metal oxide in the middle layer which is the origin of the resistive switching (RS) behaviour [1, 2]. Such resistive switching memory devices behave as memristors and can either operate upon the application of a sufficiently positive or a negative potential to effect a change in resistance (unipolar switches) or may act as bipolar switches. Bipolar resistance switching is dependent on the polarity of the applied voltage which is most often demonstrated by a potential ramp. Typical behaviour of bipolar resistance switching includes a 'figure of eight' current- potential (I-V) profile in the first and third quadrants of an I-V plot, along with a transition from a high resistance state (HRS) to a

low resistance state (LRS) or vice versa [3]. This characteristic has the potential for use as a low energy memory storage device in computing and computer memory applications.

A number of different configurations have been reported in the last decade for the production of metal oxide memristive switching devices [4,5]. These include NiO [5], ZnO [6], along with TiO_2, which is the material with the largest number of publications [7-10]. Cerium dioxide, CeO_2 is another potential semiconductor material that can either be electrochemically deposited [11] or sputter coated [12]. There are however only limited reports on the fabrication of cerium dioxide (often referred to as cerium oxide) nanostructures for use in resistive-switching devices [11, 13, 14].

Cerium, a lanthanide series element, exists in two common oxidation states, Ce^{3+} (e.g. in Ce_2O_3) and Ce^{4+} (e.g.in CeO_2). The latter is more commonly used in catalytic applications due to the higher stability of the Ce^{4+} state over the Ce^{3+} state [15]. The non-stoichiometric form of CeO_2 exhibits a broad range of stoichiometries, represented as CeO_{2-x}, where $x \leq 0.28$ [16]. The crystal structure of CeO_2 typically has a large oxygen deficiency (which increases with the decrease in the size of the nanoparticle), hence the reason for interest in the compound's nanostructure as reported by Younis et al. [11,17].

Several different mechanisms have been proposed for the operation of a memristor. One of the earliest was based on the production of high resistance (or semiconducting) nanosized layer such as TiO_2 contiguous with a conducting (low resistance) layer [18-21]. This TiO_2 layer model proposes that in order to promote a current-voltage hysteresis, the system requires a certain atomic reallocation that modulates the electronic current overtime during a potential sweep.

Depending upon the materials used, a number of different processes have also been implicated during memristive switching [22]. These include Mott (insulator-metal) transitions, Schottky barrier (semiconductor-metal) behaviour at electrode interfaces, charge trapping or de-trapping, polaron melting and ordering, electric field-induced generation of crystalline defects and the creation or destruction of conducting filaments through the thin film between both outer electrodes.

Conductive filament models have gained considerable support [8, 11, 12, 23-27]. In the Valence Change Model (VCM) it is proposed that oxygen vacancies can induce growth of a conductive strand or filament and thereby contribute to the charge transport [24-26]. In the Thermochemical Model (TCM) a high local temperature increase (up to 1000˚C) may result in formation of conductive filaments [28]. Another common filament model, the Electrochemical

Metallisation Model (ECM) is based on the oxidation/reduction of metals/ions, resulting in the formation of conductive paths between both outer electrodes. The ECM has been suggested for the operation of RS devices with Ag and Cu electrodes. One problem with such filament models is the existence of an insulating layer adjacent to one electrode making charge transport through the solid-state electrolyte extremely difficult during the application of an electrical potential.

RS devices invariably operate at room temperature where electrical conductivity (σ) in transition metal oxides, such as TiO_2 is the sum of the product of both electron (n) and hole concentrations (p) and mobility terms (μ_n and μ_p respectively) and is given by $e(n\mu_n + p\mu_p)$ where e is the elementary charge [29]. Therefore, as such devices operate under ambient conditions, the ionic conductivity contribution will be insignificant. Ionic charge transport normally occurs at high temperatures in solid state electrolytes, usually in excess of several hundred degrees Celsius. In addition, if the mechanism of RS occurred due to movement of ionic species then the current produced should be expected to decay within a few seconds after switching potential. It has been proposed for a TiO_2-based device that a constant current flow indicates p-n junction formation which plays a crucial role in the charge transport within the thin film [30]. In the case of Valence Change Memory (VCMs) memristor device models [28], oxygen vacancies formed at the anode are believed to migrate to the other electrode (cathode) and are responsible for the transition from a high resistance state (HRS) to a low resistance state (LRS) [9, 23]. Equivalent circuit models, resulting from impedance studies, have been reported for a $Pt/TiO_2/Pt$ device [31], along with a comprehensive overview of various mechanisms [32].

Thus, although several models have been suggested to explain the resistance switching behaviour of metal oxides, there is still much debate regarding the nature of the charge carriers in these devices and their operational mechanism. For example, a review of conduction mechanisms of RS devices reported a wide range of different mechanisms, sometimes a different mechanism being proposed for the same device [33]. An alternative approach is to use electrochemical principles and the concepts of an electrolytic cell involving solid-state electrolyte processes within the semiconductor interlayer and at both outer electrode interfaces [34-39].

This paper describes the fabrication of a simple macro-scale nanoparticle CeO_2-based memristive switching device using a facile drop cast method, involving a novel nanoceria synthesis. Utilising concepts concerning the operation of an electrolytic cell, together with well-known point defect models of cerium dioxide and the well-established theory of electron and

electron-hole carriers in semiconductors, a new model is proposed for the operation of cerium dioxide-based memristive switching assemblies [30, 40,41].

2. Experimental

2.1 Synthesis and characterisation of CeO_2

All chemicals were purchased from Sigma and Acros Organics and were used as received without further purification. Cerium dioxide, CeO_2 nanoparticles were prepared by precipitation in the absence of a capping agent by a novel precipitation method. Initially a solution of 0.1 mol/L $CeCl_3.7H_2O$ was prepared. This was then added dropwise to 2 mol/L ammonia solution until a precipitate formed. Finally, purple $Ce(OH)_4$ particles were produced. Excess ammonium was removed by washing with high purity water and then the supernatant liquid was removed after undergoing centrifugation several times. After that, 1 mol/L HNO_3 was added dropwise to the suspension until a stable colloid was established. The resultant solution was then heated for 30 min at 60˚C resulting in a yellow-coloured CeO_2 nanoparticle hydrosol. The hydrosol was then placed in an oven at 200˚C for 2h. Finally, the resultant powder was annealed in a furnace at a temperature of 300 °C, 600 °C, or 900 °C for 2h in order to increase the concentration of point defects. The powder was then stored in a desiccator ready for further use for a period of up to one month after production.

Physical characteristics of the synthesised nanoparticles were examined using various techniques. General morphologies were examined with a Hitachi SU 6600 FESEM scanning electron microscope (SEM) operating at 10.0 kV. A diffractometer (Siemens D-500) with a Cu anode operating at a wavelength of 0.15406 nm (Cu Kα) was used to obtain X-ray diffraction (XRD) patterns. The diffractograms were recorded in the 2θ range from 20˚ to 80˚ and the diffractometer operated at 40 kV and 30 mA. Scherrer's equation was employed to determine the primary crystallite size of a given crystal phase based on the most intense diffraction peak. The X-ray photoelectron spectroscopy (XPS) system utilised was a VG Microtech electron spectrometer at a base pressure of 1×10^{-9} mbar. The photoelectrons were excited with a conventional Mg K_α ($h\nu$ = 1253.6 eV) X-ray source and an electron energy analyser operating at a 20 eV pass energy, yielding an overall resolution of 1.2 eV.

2.2 Fabrication and Testing of Resistive Switching Devices

A suspension of CeO_2 annealed at 900˚C (0.07 g) was prepared in 2-propanol (10 cm^3). This temperature was selected due to the higher concentration of point defects as can be confirmed with XPS results. Then 10 μL of this suspension was placed on an aluminium or copper lap panel/plate (dimensions of 10 cm × 2.5 cm × 2 mm). The clear advantage of this device is its ease of construction which is readily apparent in Fig.1. This suspension layer was then allowed to dry in a fume hood and another panel (either copper or aluminium) was clamped on top of the first

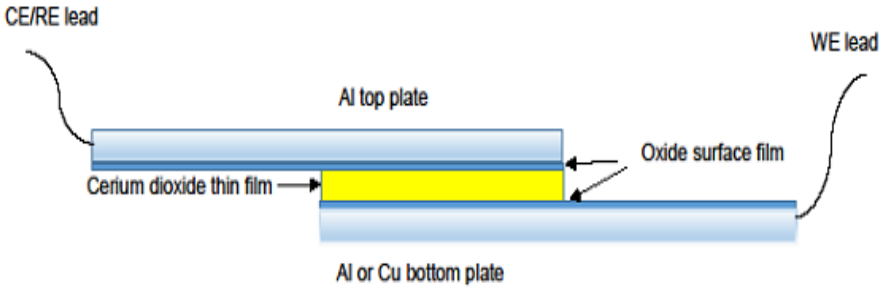

panel. An insulating pad ensured that both panels were insulated from the clamp. A computer-controlled potentiostat (CHI 600A) was used to control and monitor the device assembly where the reference and counter electrode (CE/RE) connections were linked to one panel (top electrode), while the working electrode (WE) was connected to the other (bottom electrode).

Fig.1 An expanded cross-sectional view of Al/CeO_2/Al (Cu) device (not drawn to scale). A thin film of CeO2 NP was placed between two plates which were carefully separated but connected electrically through the CeO_2 thin film interlayer forming a sandwich-like assembly.

Using this equipment, above approximately 0.6 V, the current became saturated (as it was above the potentiostat's current sensing capability). Consequently, potentials between -0.6 V and 0,6 V were typically applied in this work, in order to prevent instrument current overloading. An AFM measurement of the CeO_2 NP's layer indicated that it was 40 nm in thickness.

2.3 Electrochemical Impedance Spectroscopic Analysis

Electrochemical Impedance Spectroscopic was performed using a Solartron 1287 electrochemical system, together with a 1255B analyser and ZPlot and ZView (Scribner and Associates) software. A two-electrode configuration was adopted as in the case of the cyclic voltammogram (I-V) curves, with one electrode serving as the WE and the other a combined

CE/RE. A frequency range of 100 kHz to 0.1 Hz was employed. The instrument was calibrated with a separate equivalent circuit dummy cell using known values of each electrical component, confirming its operational performance.

3. Results and discussion

3.1 Characterisation of CeO_2

Both crystal phases and crystallinity of the synthesised nanoparticles were determined by XRD measurements as shown in Fig. 2 (a). The XRD patterns of CeO_2 powders are presented in this figure at three different annealing temperatures of 300 ˚C, 600 ˚C, and 900 ˚C respectively. The eight peaks with 2θ values of 28.6˚, 33.2˚, 47.5˚, 56.4˚, 59.2˚, 69.9˚, 77.1˚, and 79.8˚ correspond to the (111), (200), (220), (311), (222), (400), (311) and (420) planes that can be

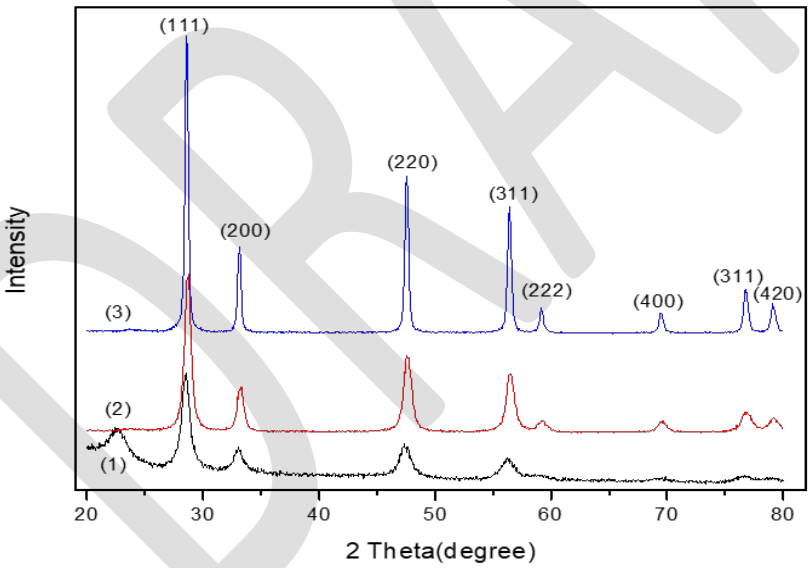

indexed as a face centred cube phase of crystalline CeO_2 [42].

Fig. 2 XRD Diffractogram of CeO_2 nanoparticles after annealing at (1) 300°C (2) 600°C and (3) 900°C respectively

XPS analysis was carried out in order to quantify the surface chemical structures and the ionisation states of the synthesised CeO_2 NPs An XPS scan is displayed in Fig. 3. Cerium 3d spectra were measured, in which the shifts in binding energies were calibrated using the C 1s peak as a reference at a binding energy of 284.8 eV. The XPS spectra of the Ce 3d level were deconvoluted and separated into Ce 3d3/2 and Ce 3d5/2 peaks. The peaks in the range 875-895 eV were assigned to the Ce 3d5/2 while peaks between 985-910 eV correspond to Ce 3d3/2 levels. The software CasaXPS® was used to carry out the calculations of integrated areas of the peaks. Peaks were fitted with a Gaussian line shape over a Tougaard background. The assignment was made of Ce^{4+} 3d component (3d5/2: 888.3 eV; 3d3/2: 906.5 eV) and Ce^{3+} 3d component (3d5/2: 879.2 eV, 891.1 eV; 3d3/2: 903.7 eV). The estimation of Ce^{3+}/Ce^{4+} ratio was found to be 59.44% for Ce^{3+} and 40.87% for Ce^{4+}. This indicates that Ce^{3+} was the predominant surface species. This is generally thought to be indicative of the presence of a substantial number of point defects, including oxygen vacancies in the underlying CeO_2 crystal structure.

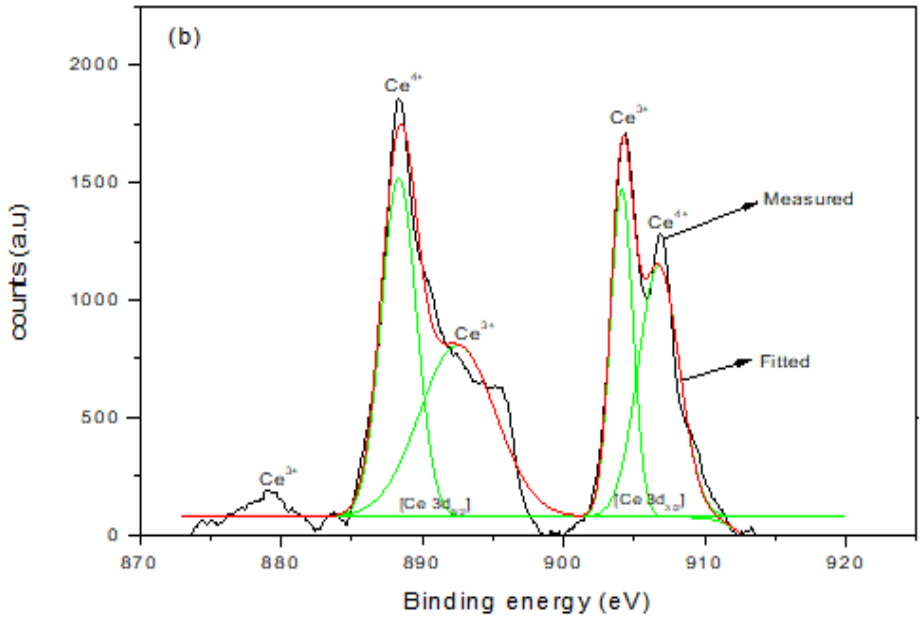

Fig. 3 XPS spectra of the as-prepared CeO_2 annealed at 900ºC.

From Scherrer's formula (Eq.1) the average crystallite size (L) may be found as:

$$L = K\frac{\lambda}{\beta}.\cos\theta \qquad (1)$$

X

where λ is the X-ray wavelength in nanometer (nm), K is a constant related to crystallite shape, normally taken as 0.9 [43]. It can be taken as 0.89 or 0.9 for Full-Width Half Maximum (FWHM) of spherical crystals with cubic unit cells. β is the peak width of the diffraction peak profile at half maximum height resulting from small crystallite size in radians. The crystallite size of CeO_2 annealed at temperatures of 300 ˚C, 600 ˚C and 900 ˚C was calculated to be 2.41 nm, 8.8 nm and 26.6 nm respectively.

3.2 Device Characterisation

SEM images provided structural and morphological insights into the CeO_2 nanoparticles. Figure 4(b) shows the CeO_2 nanoparticles are aggregated (cf Figure 4(a)). Moreover, a dense population with small nanoparticles with a mean size of 35 nm on the surface of the substrate was observed.

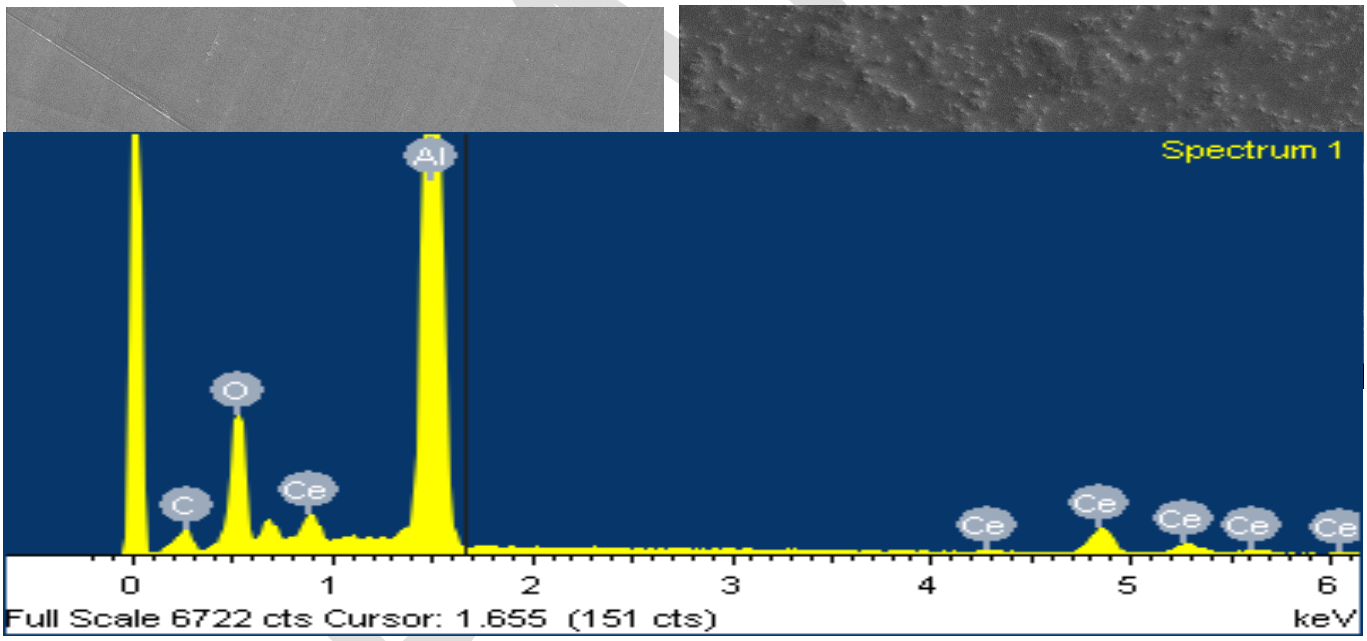

Fig. 4 (Top) SEM images of Aluminium lap shear before adding nanoceria (left). Image of Al plate after drop-casting CeO_2 NP (right). (Lower) SEM/EDS Elemental analysis of Al plate with drop cast CeO_2 NP (c) EDS data of Al/CeO_2 material.

An EDS analysis is shown in figure 4(c). This image confirms the expected composition for the Al substrate coated with CeO_2 with cerium, oxygen and aluminium all being detected, along with traces of carbon most probably from the carbon tab in the SEM chamber.

3.3 Device Behaviour and Operational Mechanism.

When cyclic voltammetry was applied to two aluminium panels clamped together, an Ohms law plot was the result. The limiting resistance was found to be 5Ω. The same resistance was found when an aluminium panel was clamped to a copper panel.

Figure 5 shows typical current-voltage (*I-V*) data of an Al/CeO_2/Cu assembly (a) in a 4 cycle cyclic voltammogram and an Al/CeO_2/Al assembly and (b) in a 12 cycle cyclic voltammogram respectively. This data was obtained from the imposition of a triangular potential sweep conducted at a scan rate of 10 mV/s over an applied potential range of -0.5 to +0.5 V. The initial potential in both cases was 0 V. This figure demonstrates classic memristive switching behaviour, with a

transition from a high resistance state (HRS, ie. low current) to a low resistance (LRS, ie. high current) state. The potential was applied to the copper electrode with respect to the aluminium electrode in Figure 5 (a). The current obtained is much larger than those often reported in the literature since most memristive switching assemblies are prepared using microfabrication methods, yielding significantly smaller surface contact areas and substantially lower currents [12, 44]. However, for our devices, the contact area is much greater, of the order of 0.5 cm^2.

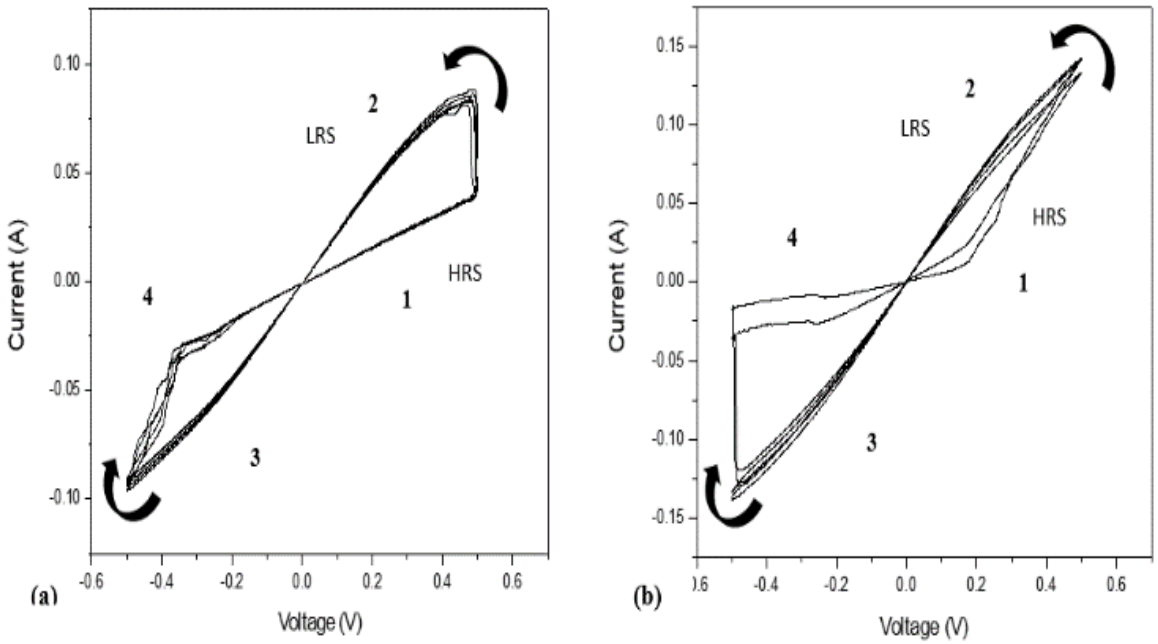

Fig. 5 A plot of current against potential displaying typical I-V behaviour of a bipolar resistive random-access memory (or memristor) of an Al/CeO2/Cu assembly, (a) the Cu panel is WE and Al is CE/RE. (b) The I-V curve of an Al/CeO2/Al assembly with Al WE and Al CE/RE. Scan rate = 10 mV/s for each

In figure 5 two different bipolar curves (*I-V*) are apparent. Figure 5 (a) (the Al/CeO_2/Cu assembly) shows a curved, largely symmetric switching behaviour, whereas in Fig. 5 (b), the Al/CeO_2/Al assembly shows a triangular curve that exhibits a clear hysteresis and asymmetric switching behaviour. For the sake of clarity, only 4 cycles are shown in Fig. 5 (a). In Fig 5 (b) the first 2 initial scans are overlaid together with the 11^{th}, and 12^{th} consecutive scans.

It is proposed that the potential energy barrier for electrons produced at a metal/semiconductor interface or junction, which is effectively a Schottky barrier, could possibly account for the difference in the bipolar curves obtained for both devices. For the Al/CeO_2/Cu assembly (Fig. 5(a)), a p-type surface copper oxide layer can occur at the Cu/CeO_2 electrode/semiconductor interface resulting in a Schottky barrier with different characteristics from its Al/CeO_2 counterpart. A Schottky barrier contact was implicated at a Cu/$BaTiO_3$ interface within a perovskite-based memristive switching device comprising of a Cu/$BaTiO_3$/Ag assembly [45].

In addition, for the Al/CeO_2/Al device (Fig 5(b)) the possible effect of the aluminium oxide passive film layer, or probably even a more complex mixed-phase (hydrated aluminium oxide)

should also be taken into account. Thus, a chemical reaction between the Al top/bottom electrode and the CeO_2 NPs could also play a role in the operation of the breakdown of the memristive switching, since this been observed experimentally for TiO_2 using advanced microscopic techniques [46]. This has been proposed by Jeong et al. [46] and Yang et al. [47] who suggested that there is an oxygen deficiency present in the comparable TiO_2 nanoparticle thin layer It is thus likely that a similar situation occurs in the case of the CeO_2 thin film layer. This contradicts the widely held view that oxygen vacancies at the metal-oxide interface play a critical role on the reversible switching between a high resistance state and a low resistance state [46, 47]. It should be noted that $Al/CeO_2/Al$ is better represented as $Al/Al_2O_3(OH)/CeO_2/Al_2O_3(OH)/Al$, e.g. with a hydrated aluminium oxide passive surface film on top of the aluminium. However, the conventional representation is $Al/CeO_2/Al$. The two assemblies shown in Figure 5 are different systems and therefore would be expected to have different electrochemical characteristics. Similar asymmetric behaviour to that shown in Fig 5(b) was demonstrated by Gale et al. for an Al/sol-gel TiO_2/Al resistive switching device [48].

Figure 6 shows an Electrochemical Impedance Spectroscopic (EIS) Bode plot recorded at an applied DC potential of 0.3 V and an AC amplitude of 10 mV. Whereas the Al/Al control showed a constant frequency-independent impedance of less than ~1 ohm, the $Al/CeO_2/Al$ device demonstrated the existence of a transition to significantly higher impedance values in the frequency range between 251 Hz to 0.79 Hz. In this frequency range the impedance rises up to ~2 X 10^6 Ω. Such behaviour was predicted by Abraham [49] who proposed a dual resistive switching between an HRS and LRS in memristor devices, similar to that observed in this work. This could be possibly be associated with changes in the operation of the Schottky barrier of the CeO_2 nanoparticles immediately adjacent to the aluminium electrode.

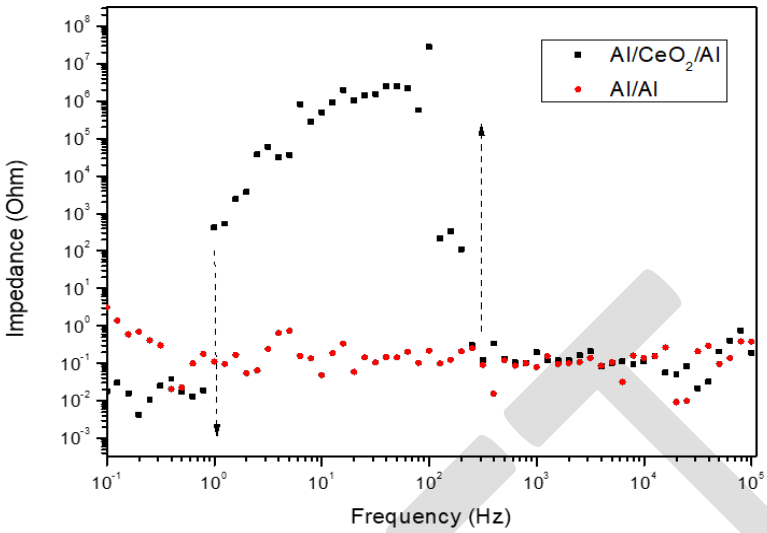

Fig. 6 EIS Bode plot of frequency against impedance displaying typical behaviour of a bipolar resistive random-access memory (or memristor) of an Al/CeO_2/Al assembly carried out at 0.3V with a ΔE of 10 mV Scanned from 100 kHz to 0.1 Hz.

Cerium dioxide nanoparticles prepared by precipitation from an aqueous salt solution followed by annealing at elevated temperature are highly non-stoichiometric in nature. Such particles contain various point defects such as oxygen vacancies, cerium vacancies and cerium interstitials [50]. In order to explain the resistive switching mechanism of CeO_2 based on the movements of electrons and holes, Kröger–Vink notation is utilised. In this notation (●●) represents a double positive charge and (e') signifies negatively charged electrons.

Thus, an oxygen ion in a normal lattice site can lead to the formation of a vacancy (with a double positive charge), along with the evolution of oxygen and the release of 2 electrons.

$$O^{x}_{o} \leftrightharpoons V_{o}^{\bullet\bullet} + 2e' + \tfrac{1}{2} O_2 \qquad (2)$$

Equation (2) explains why the presence of oxygen vacancies has been attributed to an n-type CeO_2 semiconductor [51-53]. The notation of the lattice components according to both the Kröger-Vink notation used in solid state physics and the traditional chemical notation are presented in Table 1 for CeO_2, adapted from an analogous oxide material, TiO_2 [54].

Table 1. Notations used to denote various CeO_2 lattice defect species along with the Kröger-Vink notation and net charge. Adapted from the semiconductor material TiO_2 [54].

Traditional Notation	Physical Presence	Kröger-Vink Notation	Net Charge
Ce_{Ce}^{4+}	Ce^{4+} ion in cerium lattice site	Ce_{Ce}^{x}	Neutral
Ce_{Ce}^{3+}	Ce^{3+} ion in the Cerium lattice site (quasi-free electron)	Ce_{ce}'	-1
V_{Ce}	Cerium vacancy	V_{Ce}''''	-4
Ce_i^{3+}	Ce^{3+} ion in interstitial site	$Ce_i^{\bullet\bullet\bullet}$	+3
Ce_i^{4+}	Ce^{4+} ion in interstitial site	$Ce_i^{\bullet\bullet\bullet\bullet}$	+4
O_O^{2-}	O^{2-} ion in oxygen lattice site	O_O^{x}	Neutral
V_O	Oxygen vacancy	$V_O^{\bullet\bullet}$	+2
O_O^{-}	O^{-} ion in oxygen lattice site (quasi-free electron-hole)	$h^{\bullet}$	+1

Figures 7 and 8 show the currents obtained from the application of selected constant potentials (in 0.1 V increments) to the copper/aluminium electrode with respect to the aluminium electrode, for the $Al/CeO_2/Cu$ assembly and for the $Al/CeO_2/Al$ assembly respectively. The current evolution at each fixed potential was recorded for a period of 10 s. The resulting constant currents indicate resistive behaviour. This confirms that the current is produced by the rapid movement of electrons or holes rather than by ionic species as it not dependent on $t^{-1/2}$. However, the current behaviour is different when a positive potential is applied compared to when a negative potential is applied. In the case of the high negative potentials (-0.4 V and -0.5 V), a slight initial current decay is evident before a steady-state current is attained as is evident in figure 7.

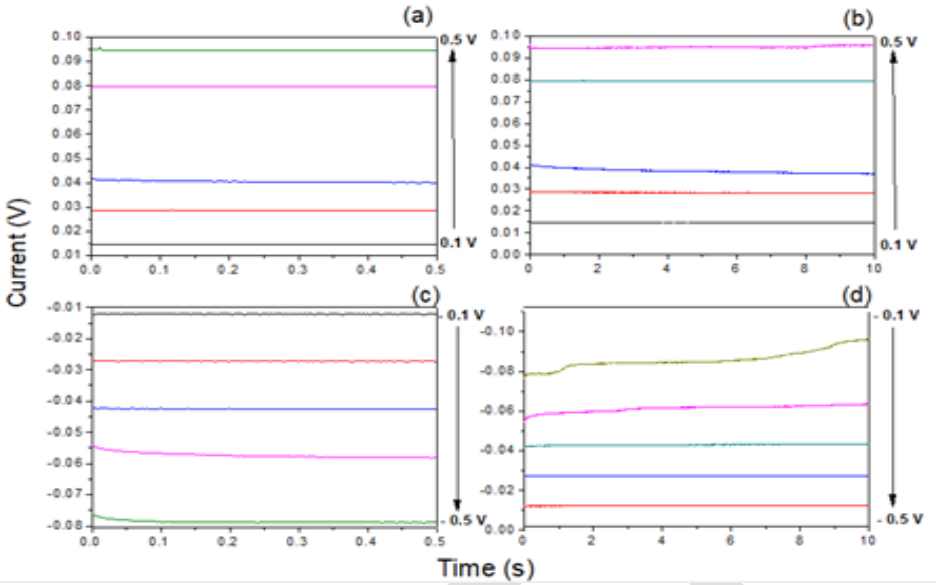

Fig. 7 Current transients at fixed potentials for 10s and 0.5s in 0.1 V steps ranging from 0.1 V to 0.5 V on top side (a) and (b) respectively and -0.1 V to -0.5 V on the bottom side for

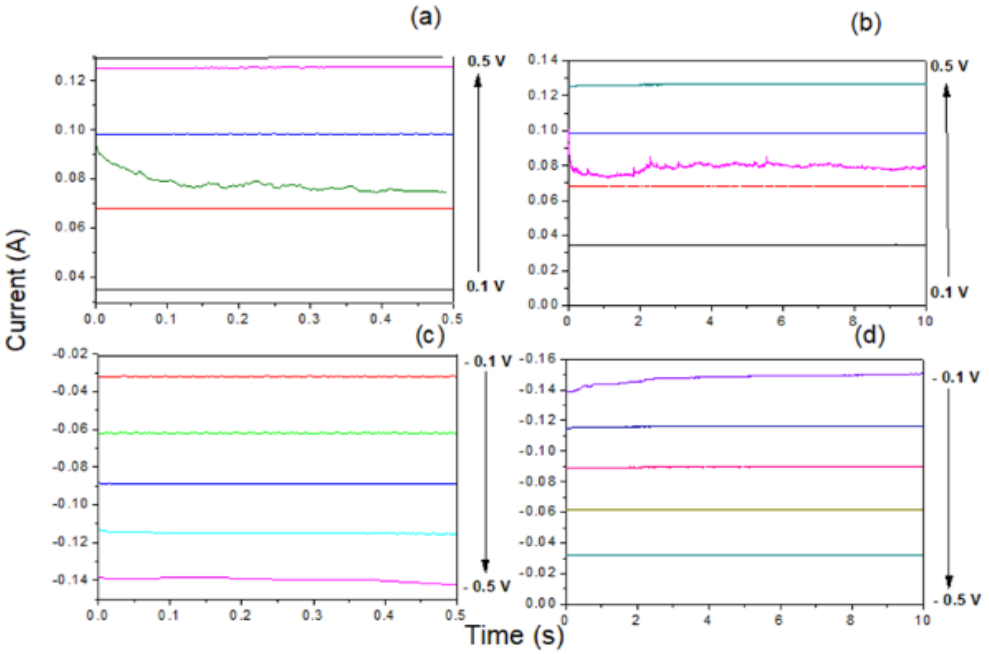

Al/CeO2/Cu (c) and (d). This data comes from the same device as that measured in Fig. 5 (a)

Fig. 8 Current transients at fixed potentials for 10s and 0.5s in 0.1V steps ranging from 0.1V to 0.5V on top side (a) and (b) respectively and -0.1V to -0.5V on bottom side for Al/CeO2/Al (c) and (d). This data comes from the same device as that measured in Fig. 5 (b).

Figure 8 displays the corresponding current-time behaviour for the Al/CeO_2/Al device, where once again the resulting constant current indicates a non-diffusional behaviour. The current is essentially steady, apart from the most positive potential, with some current noise evident at 0.3 V. Such constant currents are not observed for the movement of ionic species, only at p-n junctions, where the movement of electron and holes occurs [30]. As can be observed in Figures 7 (b), 8 (b) and 7(d), 8(d), the current is constant for the first few milliseconds. Such a linear current–time dependence supports the notion that a diffusion-controlled process involving ionic species is not occurring at the Al and Cu outer electrodes.

Rather than a mechanism involving ionic movement, it is suggested instead that in these macro-scale memristive switching devices, electron and hole movement forms a p-n junction which is forward-biased. Ultimately a low resistance state is attained and eventually a constant current observed at both positive and negative fixed potentials. Therefore when the thin film of CeO_2 is placed between two outer electrodes in a memristor configuration (figure 1) and a positive potential is applied (region 1 in Figure 5 (a) and (b)), oxidation happens at the anode (equation (2 or 3)) to form a p-type CeO_2 since the $V_o^{\bullet\bullet}$ remain, while the electrons pass into the electrode. In figure 5 (a) and (b) the initial potential is zero volts and region 1 corresponds to the initial sweep. It can be seen that the current is small since the CeO_2 is mostly resistive at this stage. However, at the anode, the following oxidation reaction takes place (analogous to equation (2)):

$$O^{2-} \rightarrow O_2 + 2\,e^- \quad (3)$$

Fig. 9 Schematic representation of the transition from HRS semiconductor in region 1 (and region 4) of I-V scans depicted in Fig 5 (top) to conducting LRS (bottom) responsible for the increase in current in region 2 (and region 3) of Fig 5.

This leads to a p-type semiconductor forming close to the anode. Such generation of oxygen at the anode of memristive switching devices has been seen experimentally [47,48, 56]. This reaction can be considered as a half cell reaction, typical of that occurring in an electrolytic type of electrochemical cell. It has also been suggested that oxygen species can react directly with Al to form oxygen vacancies and an aluminium oxide; thus [48, 55]

$$2/3\ Al + O \rightarrow V_O^{\bullet\bullet} + 2e^- + 1/3\ Al_2O_3 \quad (4)$$

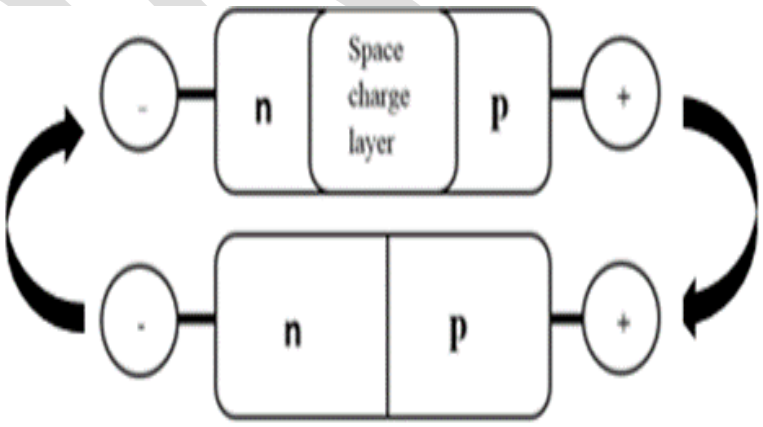

Simultaneously an electrochemical reduction reaction occurs at the cathode yielding an n-type region (equation 5). Such a reduction process (equation 5) has previously been reported by Younis et al. (11] and by Gao et al [22], both for CeO_2.

$$Ce^{x}_{Ce} + e^- \rightarrow Ce_{ce}' \quad (5)$$

In region 1 in figure 5 (a) and (b) at this stage, there is a movement of O^{2-} toward the anode or the movement of oxygen vacancies toward the cathode. Previous models in a TiO_2 memristive switching device comprise a conducting region adjoining an insulating region without acknowledging the reduction of Ti^{4+} forming TiO_{2-x}. However, as shown in Figure 9 (top) there is still an insulating region between the two semiconducting regions, which limits the current to low values, indicative of a high resistance state (HRS). As the potential is swept the semiconducting regions extend and once they meet, as shown in the lower part of Figure 9, a forward biased p-n junction is formed and the current thus increases dramatically [30, 40]. It has been proposed that the transition from n-type to p-type conduction can take place at low temperatures [57]. The creation of a p-n junction has been reported in a CeO_{2-x} electrolyte [58].

In contrast ionic conduction only becomes significant at high temperatures, often above 500˚C which further supports the notion that the charge is carried by electrons and holes, rather than by ions in these devices operating at ambient temperatures [57]. As a consequence of this, a constant current is obtained at a constant potentials as displayed in Figures 7 and 8. If mass transport of O^{2-} was responsible for the measured current shown in Figures 7 and 8 a decrease in current would be expected as a consequence of the consumption of O^{2-} during the scan/device operation.

As the potential is swept back to zero volts (region 2 in Figure 5 (a) and (b)) there is still an enhanced current (LRS); however, since the driving force decreases (e.g. the potential becomes less), there is a decrease in the current. Once the polarity is changed, there is an immediate reversal of reactions (3) and (5). As the potential is swept more negative the rates of the two reactions increase and there still is an enhanced current as the majority of the device is still semiconducting. In region 3, the semiconducting regions that were created in regions 1 and 2 are slowly converted back to an insulating state. At the switching potential, corresponding to a decrease in the concentration of O_2 and Ce_{ce}', the current drops dramatically as the device returns to its insulating state (HRS). In region 4 the current is small, since the device is primarily now in an insulating state.

The *I-V* plot shown in Figure 5 (b) is not symmetric; this has also been reported in other memristor devices produced micro lithographically [44, 45]. Indeed, a characteristic of our device is its simplicity; it can be produced without vacuum or microlithographic techniques. Thus, it is a platform that can be modified readily using inkjet [8] or screen-printing techniques [10] or other methods including spin coating, spray coating and blade coating [58]. In fact, most memristive

switching systems reported in the literature use small scale electrodes (of the order of micrometres or smaller) separated by thin (nanometre-sized) layers. In these assemblies' defects such as surface defects, dislocations and grain boundaries may all play a significant role in their operation [60,61]. It is also worth noting that the imposition of a high electric field (e.g. more than 10^7V/m) can lead both to the creation of oxygen vacancies (equation 2) and to the movement of ionic and defect species in close proximity to an electrode, thereby promoting the reactions described in equations 2 to 5. Evidence for this non-thermally induced point defect production and response to a high electric field has come from studies involving cerium oxides [62, 63]. The occurrence of high temperatures due to joule heating or some other localised thermal effect was refuted by Munjal and Kharee [55] in their work and also by Li et al [63] in their study of CeO_2 thin film memristive behaviour.

While memristive switching behaviour is seen for the initial scans in Fig. 5, it is not shown after repeated consecutive cycles. Eventually the response changes to that of a pure resistor, indicating a change in the mechanism to ohmic conduction, as reported elsewhere [3]. In this case it is possible that in the absence of a high formatting or SET potential (larger than 1 V) the levels of defects such as oxygen vacancies created within the high elctric field were insufficient to sustain the memristive switching in the macro-scale CeO_2 device, resulting in destruction of the p-n junction over time. Alternatively as the device studied in this work was exposed to laboratory air, it is also feasible that oxygen and moisture access may have played a role in the loss of memristive switching behaviour through alteration of the electrodes' surface chemistry over time [64]. Others have however reported high stability of more conventional CeO_2 based memristive switching assemblies [14].

4. Conclusions

Crystalline cerium dioxide nanoparticles were prepared by a facile precipitation method and characterised using a variety of methods. When drop-cast as a thin film and placed between two conductive Al/Al or Al/Cu plates in a macro-scale assembly the prepared nanoceria exhibits resistive switching behaviour with a certain HRS/LRS characteristic. The memristive-switching device behaviour is explained in terms of an electrolytic cell involving point defect chemistry and semiconductor electrochemistry utilising electron and hole movement within the CeO_2 thin film interlayer. This new electrolytic cell/semiconductor model accounts for the initial changes in the current-potential behaviour of such devices, which may decay over time back to a normal ohmic

resistive state. This decay is possibly accounted for by the destruction of a conductive p-n junction over time, which is more readily apparent in a macro-scale device.

Conflicts of Interest

There are no conflicts of interest to declare.

Acknowledgements

The authors gratefully acknowledge the award of a DIT Fiosraigh Dean of Graduate Studies award to R C de Carvalho and participation in COST Action MP 1407 (e-MINDS).

References

1 E. Gale, *Semicond.Sci. Tech.* 2014, **29**, 104004

2 A. Younis, D.Chu, I. Mihail, S. Li, *Appl. Mater. Interf.* 2013, **5,** 9429

3 J. Yoo, K. Lee, A.Tighineanu, P. Schmuki, *Electrochem. Comm* 2013, **34** , 177

4 A Sawa *Mats Today* 2008 **11**, 6 28

5 S. Seo *Appl. Phys. Lett.* 2004, **85,** 5655

6 B Gao, S Yu, N Xu, L F Liu, B Sun, X Y Liu, R Q Han, J F Kang, B Yu, Y Y Wang, *IEEE Electronic Devices Meeting*, Dec 2008, 1

7 D. Chu, A. Younis, S.Li, *J. Phys. D: Appl. Phys*. 2012, **45,** 355306

8 Z. Yu, X Qu, W. Yang, J. Peng, Z. Yu, *J. Alloys Compounds* 2016, **688,** 294

9 N. Duraisamy, N.M. Muhammad, H.-C. Kim, J.-D. Jo, K.-H. Choi, *Thin Solid Films* 2012, **520,** 5070

10 D.H. Lien, Z.K. Kao, T.-H Huang, Y.C. Liao, S.C. Lee, J.H. He, *ACS Nano* 2014, **8,** 7613

11 A. Younis, D. Chu, S Li, *J. Phys. D: Appl. Phys.* 2012, **45**, 355101

12 A. Younis, L. Zhang, D. Chu, S. Li, *Appl. Phys. Lett* 2016, **108,** 033506

13 M. Ismail, E. Ahmed, A. M. Rana, F. Hussain, I. Talib, M. Y. Nadeem, D. Panda, N.A. Shah, *ACS Appl. Mater, Interfaces* 2016, **8,** 6127

14 C. C. Hsieh, A. Roy, A. Rai, Y. F. Chang, S. K. Banerjee, *Appl. Phys. Lett*. 2015, **106,** 173108

15 W. Haynes, T. Bruno and D. Lide, *CRC Handbook of Chemistry and Physics, CRC Press*, (2015) Boca Raton, FL, 96th Ed

16 K. Ghillanyona, D. Galusek, *Ceramics Sci Tech Mat Prop* 2011, **2,** 1125

17 A. Younis, D. Chu and S. Li, *Functionalized Nanomaterials* 2016, **3,** 1064

18 D.B. Strukov, R.S Williams, *Appl. Phys*. 2009, **94,** 515

19 D.B.Strukov, G.S.Snider, D.R.Stewart, R.S.Willians, *Letters, Nature* 2008, **453,** 80

20 T.D.Dongale, K.P.Patel, P.K.Gaikwad, R.K.Kamat, *Mater. Sci. in Semicond. Proc.* 2015, **38,** 228

21 L.Chen, C.Li, T.Huang, H.G. Ahmad, Y.Chen. *Phys. Lett. A.* 2014, **378,** 2924

22 P.Gao, Z. Wang, W Fu, Z. Liao, K.Liu, W.Wang, X.Bai, E.Wang, *Micron* 2010, **41,** 301

23 C.Ye, J.Wu, G.He, J.Zhang, T.Deng, P.He, H.Wang, *J.Mat. Sci. Tech*. 2016, **32,** 1

24 F.Pan, S.Gao, C.Chen, C.Song, F.Zeng, *Mater. Sci. Eng. Res* 2014, **83,** 1

25 V. Senthilkumar, A. Kathalingam, V. Kannan, J.K Rhee, *Microelectronic.Eng.* 2012, **98,** 97

26 K.Szot, W.Speier, G.Bihlmayer, R.Waser, *Nature Materials*, 2006, **5,** 312

27 T Salaoru, A Prodromakis, A Khiat, C Toumazou, *Appl. Phys. Lett* 2013, **102**, 13506

28 D.Kalaev, E.Yalon, I.Reiss, *Solid State Ionics* 2015, **276,** 9

29 J. Nowotny, M.A Alim, T Bak, M S Idris, M. Ionescu, K.Prince, M.Z Sahdan, K. Sopian, M.A.M Teridi, W. Sigmund, *Chem Soc Reviews* 2015, **44,** 8424

30 R.C. de Carvalho, A.J. Betts, J.F. Cassidy, *J Solid State Electrochem* 2019, **23,** 1939

31 M.H.Lee, K.M.Kim, G.H.Kim, J.Y. Seok, S.J.Song, J.H.Yoon, C.S.Hwang, *Appl. Phys. Lett*, 2010, **98,** 152909

32 J. Blasco, N.Ghenzi, J.Sué, P.Levy, E.Miranda, *Microelectron. Reliability* 2015, **55,** 1

33 E.W Lim, R. Ismail, *Electronics* 2015, **4,** 586

34 L.C.T Shoute, N.Pekas, Y.Wu, R.L.McCreery, *Appl. Phys. A* 2011, **102,** 841

35 J.Wu, R.L.McCreery, *J.Electrochem. Soc*. 2009, **156,** 29

36 J.F.Cassidy, D.Fox, A.J.Betts, *J. Solid State Electrochem*. 2016, **20,** 1229

37 I Valov, ChemElectroChem, 2014, **4**, 26-36

38 W Sun, B Gao, M Chi, Q Xia, J. Yang, H Qian H Wu, Nature Comms 2019, **10**, 3453

39 R Waser, J Nanosci Nanotech 2012, **12**, 7628

40 R Waser, Dittmann, G Staikov and K Szot, *Advan. Materials* 2009, **31,** 2632

41 P. S. Madhusudana, K. Mohanta, S. K. Batabyal, *J Solid State Electrochem* 2019, **23**, 1307

42 H. Balavi, S.S.Isfahani,M.M. Zindabad, M.Edrissi, *Powder Technol* 2013, **249,** 549

43 A. Monshi, M.R.Foroughi, M.R.Monshi, *World J. of Nano Sci. and Eng.* 2012, **2,** 154

44 E. Gale, R. Mayne, A. Adamatzky, B.de Lacy Costello, *Mater. Chem. Phys*. 2014, **143,** 524

45 L. J. Wei, Y. Yuan, J. Wang, H. Q. Tu, Y. Gao, B. You and J. Du, *Phys. Chem. Chem. Phys*, 2017, **19,** 11864

46 H.Y.Jeong, J. Y. Lee, S.Y. Choi, J. W. Kim. *Applied Phys Letters* 2009, **95,** 162108

47 J. J. Yang, F. Miao, M. D. Pickett, D. A. A. Ohlberg, D. R. Stewart, C. N. Lau, and R. S. Williams, *Nanotechnology* 2009, **20,** 215201

48 E. Gale, D. Pearson, S. Kitson, A. Adamatzky, B.de Lacy Costello, *Mater. Chem. Phys.* 2015, **162,** 20

49 I Abraham, *Sci Reps*, 2018, **8**, 10972

50 A.Tschope, W.Liu, M.F.Stephanopoulos, J.Y.Ying, *J. Catalysis* 1995, **157,** 42

51 Y-M Chiang, E B Lavik, I Kosacki, H L Tuller, J Y Ying, *Appl. Phys. Lett.* 1996, **69,** 185

52 S Gangopadhyay, D M Frolov, A Masunov, S Seal, *J Alloy Compd* 2014, **584**, 199

53 K Kaviyarasu, Xolilie Fuku, Genene T Mola, E Manikandan, J Kennedy, M Maaza, Mats. Letts, 2016, **183,** 351

54 M.K. Nowotny, L.R. Sheppard, T.Bak and J. Nowotny, *J. Phys. Chem. C.* 2008, **112,** 5275

55 S Munjal and N Khare, Sci Reports, 2017, **7**, 12427

56 C. S. Dash, S Sahoo, S Prabaharan, *Solid State Ionics* 2018, **324,** 218

57 J. A. Kilner, *Solid State Ionics* 2000, **129,** 13

58 B Wang, B. Zhu, S Yun, W Zhang, C Xia, M Azfal, Y Cai, Y Liu, Y Wang H Wang, NPG Asia Mater, 2019, **11,** 51

59 Y Shan, Z Lyu, X Guan, A Younis, G Yuan, J Wang, S Li T Wu *Phys. Chem. Chem. Phys*., 2018, **20**, 23837

60 Y Ding, Y Chen, K C Pradel, M Liu, Z Lin Wang, J Appd Phys 2016, **120**, 214302

61 L.N. Liu, C.H. Zang, B. Wang, W. Su, H.Y. Xiao, D.M. Zhang, Y.S.Zhang, Vacuum, 2020, **173**, 109128

62 P. Gao, Z. Kang, W. Fu, W. Wang, X. Bai, E. Wang, J. Am. Chem. Soc. 2010, **132**, 12, 4197-4201

63 X. Li, K. Qi, M. Sun, Q. Huang, Z. Xu, W. Wang, X. Bai, Appl. Phys. Lett. 2015**, 107**, 211902

64 S. Tappertzhofen, I. Valov, T. Tsuruoka, T. Hasegawa , R. Waser, M. Aono, ACS Nano 2013, **7**, 7, 6396-6402